Supplementary Information

Selenium doping induced phase transformation and interlayer expansion boost the zinc storage performance of molybdenum disulfide

Mengfan Niu [a], Wenli Xin [a], Lei Zhang [a], Min Yang [c], Yaheng Geng [a], Xilin Xiao [a], Hui Zhang [a], and Zhiqiang Zhu [a,b,*]

[a] *State Key Laboratory of Chemo/Biosensing and Chemometrics, College of Chemistry and Chemical Engineering, Hunan University, Changsha 410082, China*
[b] *Greater Bay Area Institute for Innovation, Hunan University, Guangzhou 511300, China*
[c] *School of Chemistry, Xiangtan University, Xiangtan 411105, China*

E-mail addresses: zqzhu@hnu.edu.cn

Experimental Section

Synthetic procedures of MoS$_{2-x}$Se$_x$/rGO. In a typical procedure,[1] 0.75 mmol Na$_2$MoO$_4$·2H$_2$O and 1.4 mmol CH$_4$N$_2$S were added into 20 mL graphene oxide (GO, 3.5 mg mL^{-1}) suspension, which was sonicated for 2 h and intensively stirred for 10 h to form homogeneous solution A. Then 0.076 mmol selenium powder was added to 3 mL N$_2$H$_4$·H$_2$O (80%) and stirred for 1 h at 70 °C to form solution B. Next, solution A was mixed with solution B under stirring for 3 h, which was then transferred to a 50 mL Teflon-lined stainless-steel autoclave and maintained at 180 °C for 24 h. After cooling to room temperature, the MoS$_{1.8}$Se$_{0.2}$/rGO was washed with deionized water until neutral and dried by lyophilization. The S/Se ratios of MoS$_{2-x}$Se$_x$/rGO were optimized by varying the molar ratios of CH$_4$N$_2$S and Se powder (39:1 and 9:1), and the corresponding products were denoted as MoS$_{1.9}$Se$_{0.1}$/rGO and MoS$_{1.5}$Se$_{0.5}$/rGO, respectively. In comparison, MoS$_2$/rGO and MoSe$_2$/rGO were synthesized by the same procedure without the addition of Se powder and CH$_4$N$_2$S, respectively.

Material characterization. The morphologies of the samples were observed by transmission electron microscope (TEM, FEI-Tecnai G2 TF20) and scanning electron microscope (SEM, TESCAN MIRA3) equipped with energy-dispersive X-ray spectroscopy (EDS). Raman spectra were recorded by Raman microscope (Renishaw inVia) with a laser wavelength of 532 nm. The crystal structures were characterized by X-ray diffraction (XRD, Bruker D8 ADVANCE, Cu Kα radiation). The rGO contents of the samples were detected by thermogravimetric analyzer (TG, Labsys Evo, Setaram). The chemical composition of the samples was analyzed by X-ray photoelectron spectroscopy (XPS, Kratos Axis Ultra DLD, Japan).

Electrochemical Characterizations. The MoS$_{2-x}$Se$_x$/rGO active materials, super P carbon and polyvinylidene fluoride (PVDF) were mixed by weight ratio of 7:2:1 and well-dispersed in N-methyl-pyrrolidone (NMP). The mixture was uniformly pasted on a titanium foil and dried in a vacuum oven at 60 °C over night to fabricate the working electrode. Finally, the electrodes were cut into Φ10 mm rounds with 1–1.5 mg cm^{-2} active materials mass loading. CR2032 coin cells were assembled by using the working electrode as the cathode, glass fiber as the separator, 3 M Zinc trifluoromethanesulfonate (Zn(CF$_3$SO$_3$)$_2$) aqueous solution with 5 vol% polyethylene glycol (PEG) as the electrolyte, and Zn metal as the anode. The charge/discharge measurements and galvanostatic intermittent titration technique (GITT) experiments were carried out on the LAND battery testing system (CT2001A Wuhan LAND Electronics Co., Ltd., China) within the voltage window of 0.2–1.3 V. The cyclic voltammetry (CV) and electrochemical impedance spectroscopy (EIS) of batteries were characterized by electrochemical workstation (Admiral SquidStat Plus) at room temperature. The three-electrode system with dilute H$_2$SO$_4$ (pH≈3.5) as the electrolyte, MoS$_{1.8}$Se$_{0.2}$/rGO as the working electrode, Ti as the control electrode, and Ag/AgCl electrode as the reference electrode was used to investigate the H$^+$ insertion behavior.

Computational Methods. All the calculations results are based on the density functional theory (DFT). The Geometry Optimization of the system used Cambridge Sequential Total Energy Package (CASTEP) module. The generalized gradient approximation (GGA) of Perdew-Burke-Ernzerhof (PBE) functional was employed to describe the exchange–correlation potential during structural optimization of MoS_2 crystals. The first Brillouin zone was sampled by $1 \times 1 \times 1$ Monkhorst Pack k-point grid. The cutoff energy of plane wave basis was set to be 571.4 eV and the self-consistent field tolerance was 1.0×10^{-6} eV atom^{-1}. The Heyd-Scuseria-Ernzerhof (HSE) hybrid density functional was used to calculate the density of states (DOS) and band structure.
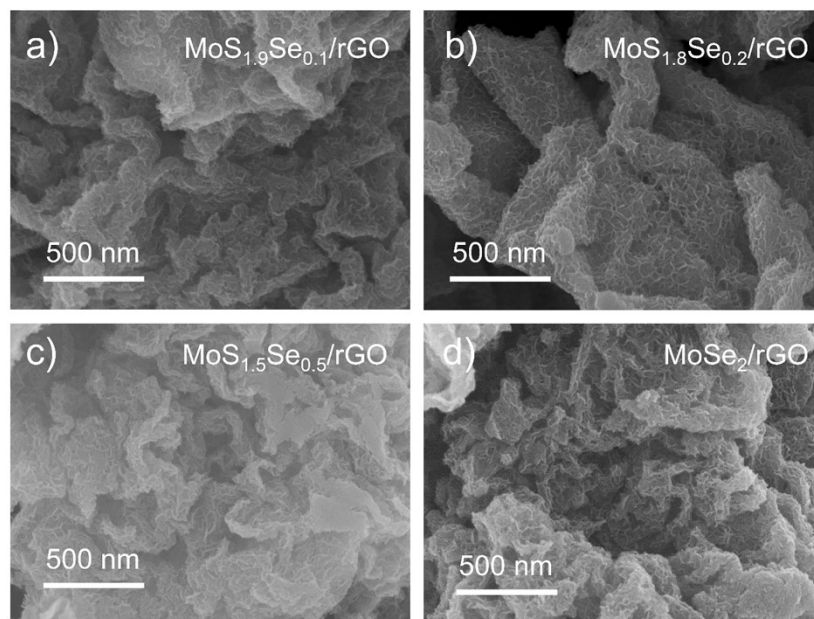
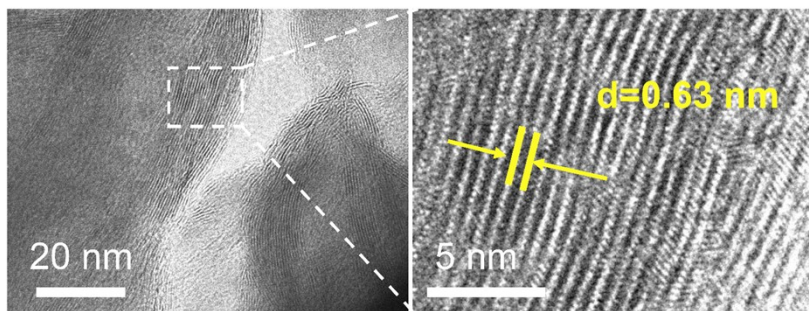**Fig. S1.** FESEM images of (a) MoS_2/rGO, (b) $MoS_{1.9}Se_{0.1}$/rGO, (c) $MoS_{1.5}Se_{0.5}$/rGO, and (d) $MoSe_2$/rGO.

Fig. S2. TEM images of MoS$_2$/rGO.

Table S1. Calculated contents of different elements in $MoS_{1.9}Se_{0.1}/rGO$, $MoS_{1.8}Se_{0.2}/$

Samples	C (%)	Mo (%)	S (%)	Se (%)	S: Se
$MoS_{1.9}Se_{0.1}$	48.15	18.45	31.52	1.88	16.8
$MoS_{1.8}Se_{0.2}$	55.53	15.98	26.14	2.52	10.4
$MoS_{1.5}Se_{0.5}$	54.22	14.37	22.60	8.8	2.6

rGO and $MoS_{1.5}Se_{0.5}/$ rGO.
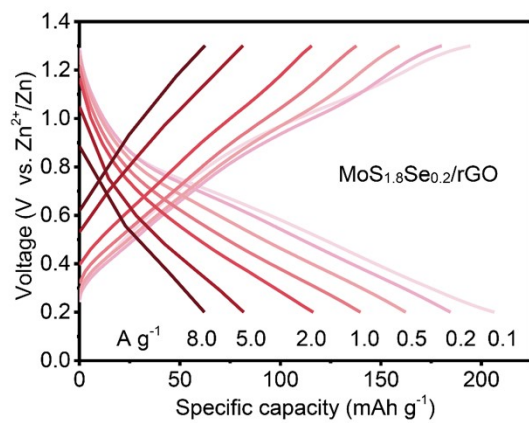
Fig. S3. Ccharge/discharge curves of $MoS_{1.8}Se_{0.2}/rGO$ at different current densities.

Table S2. The fitted values according to the EIS of $MoS_{2-x}Se_x/rGO$.

Cathodes	R_s (Ω)	R_{ct} (Ω)
MoS_2/rGO	20.5	138.6
$MoS_{1.9}Se_{0.1}/rGO$	19.8	56.4
$MoS_{1.8}Se_{0.2}/rGO$	20.9	30.1
$MoS_{1.5}Se_{0.5}/rGO$	17.3	45.9
$MoSe_2/rGO$	28.2	90.3
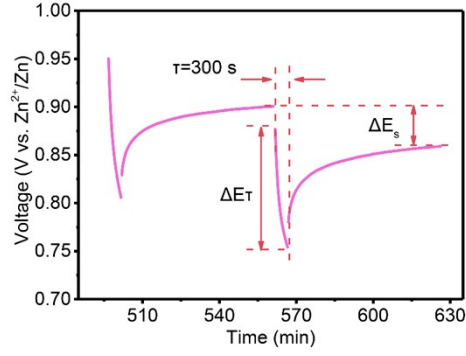
Fig. S4. Voltage profiles before, during, and after a constant current pulse at 0.9 V for the $MoS_{1.8}Se_{0.2}$/G electrode.

The ions diffusivity (D^{GITT}) can be calculated by the following equation:[2]

$$D^{GITT} = \frac{4L^2}{\pi\tau}(\frac{\Delta E_S}{\Delta E_\tau})^2$$

Where t and τ represent the duration pulse (s) and relaxation time (s), respectively. L corresponds to the ion diffusion length (equal to the thickness of the electrode). ΔE_s is the steady-state potential change (V) by the current pulse. ΔE_t is the voltage change (V) during the constant current pulse (eliminating the voltage changes after relaxation time).
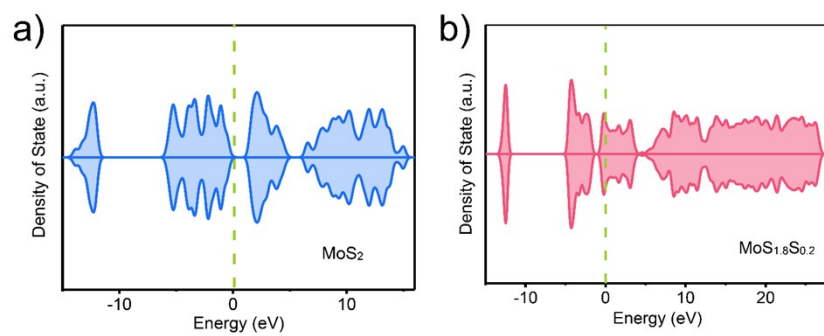
Fig. S5. Calculated density of states of (a) MoS_2 and (b) $MoS_{1.8}Se_{0.2}$.

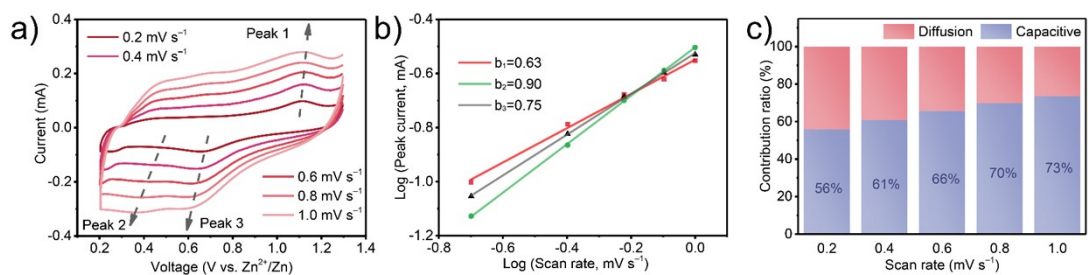**Fig. S6.** (a) CV profiles of MoS$_2$/rGO at various scan rates from 0.2 to 1.0 mVs^{-1}, and (b) the b-value determination through the relationship of peak currents and scanning rates. (c) Capacitive and intercalation contribution to the total stored capacity of the MoS$_2$/rGO electrode at different scan rates.
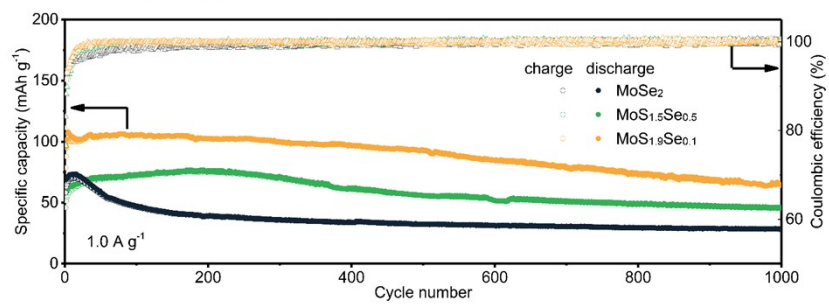
Fig. S7. Long-term cycling stability and Coulombic efficiency of $MoS_{1.9}Se_{0.1}$/rGO, $MoS_{1.5}Se_{0.5}$/rGO and $MoSe_2$/rGO at 1.0 A g^{-1}.
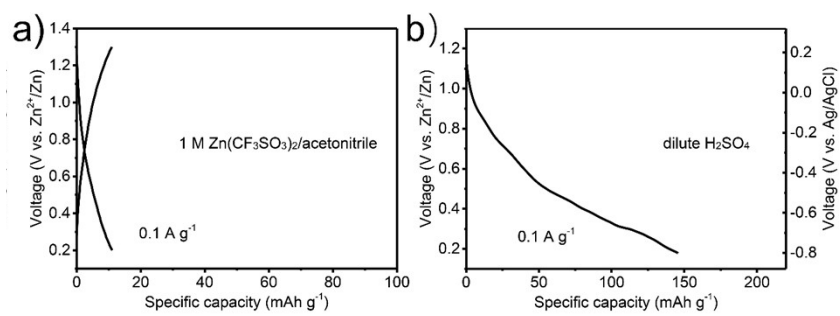
Fig. S8. (a) Charge/discharge curves of MoS_2/rGO at 0.1 A g^{-1} in 1 M $Zn(CF_3SO_3)_2$/acetonitrile. (b) Discharge curve of MoS_2/rGO at 0.1 A g^{-1} in dilute H_2SO_4 (pH≈3.5) researched by a three-electrode cells.

Reference

1   H. Li, R. Gao, B. Chen, C. Zhou, F. Shao, H. Wei, Z. Han, N. Hu and G. Zhou, Vacancy-rich MoSSe with sulfiphilicity−lithiophilicity dual function for kinetics-enhanced and dendrite-free Li-S batteries, *Nano Lett.*, 2022, **22**, 4999–5008.

2   H. Geng, M. Cheng, B. Wang, Y. Yang, Y. Zhang and C. C. Li, Electronic structure regulation of layered vanadium oxide via interlayer doping strategy toward superior high-rate and low-temperature zinc-ion batteries, *Adv. Funct. Mater.*, 2020, **30**, 1907684.